Quantitative framework for photoemissive materials: From bialkali-antimonide synthesis to performance in superconducting RF electron injectors

Jonas Dube,[*,‡] Chen Wang,[†] Emily Jayne Brookes,[*] Axel Neumann, Guido Klemz, Ezgi Ergenlik, Pablo Echevarria, Andriy Ushakov, Thorsten Kamps,[*] and Julius Kühn[§]
Helmholtz-Zentrum Berlin für Materialien und Energie GmbH, Hahn-Meitner-Platz 1, 14109 Berlin, Germany

(Received 2 April 2026; accepted 23 June 2026; published 10 July 2026)

Photoemissive materials are central to a wide range of technologies, including ultrafast imaging, low-light detection, and accelerator-based light sources, where they determine the fundamental performance limits of these instruments. Despite their importance, establishing quantitative links between material synthesis, electronic structure, intrinsic photoemission properties, and device performance remains a major challenge. Here, we present a comprehensive study that bridges these aspects for Na–K–Sb photocathodes, combining controlled thin-film growth, *in situ* spectroscopic analysis, photoemission characterization, and investigation of the operational performance. We developed a reproducible synthesis method yielding highly homogeneous films with quantum efficiencies up to 7.5% at 520 nm and a stoichiometry close to the predicted optimum. Electronic structure and photoemission properties were analyzed in a dedicated laboratory environment. Furthermore, we demonstrate the successful operation of these photocathodes in a superconducting radio-frequency photoinjector, where the photocathodes are exposed to extreme conditions, forming a particularly stringent test environment. The operational performance was analyzed over several weeks, including detailed investigation of the degradation and recovery mechanisms associated with gas exposure and electron back-bombardment. The photoemissive threshold energy was identified as a bridging parameter connecting electronic structure, photoemissive key parameters, and the degradation state. The approach provides general design principles for the development and integration of photoemissive materials across a broad range of applications. Together, these results establish a quantitative framework linking synthesis, electronic structure, and operational performance in photoemissive materials.

DOI: 10.1103/d2s8-7pt8

I. INTRODUCTION

Photoemissive materials are used to convert photons to electrons and are a key component in a wide range of modern technologies, including low-light detection, ultrafast spectroscopy, electron microscopy, and accelerator-based light sources [1–4]. Their performance is governed by a complex interplay of electronic structure, surface chemistry, and transport processes, which together determine central figures of merit such as quantum efficiency (QE), energy spread, and operational stability [5,6]. More broadly, they represent a class of functional materials where macroscopic device performance is highly sensitive to microscopic material properties and preparation conditions.

A central challenge in the development of such materials lies in establishing robust and predictive links between synthesis, photoemission properties, and performance in realistic operating environments [7,8]. While significant progress has been made in controlling growth processes and in characterizing materials using spectroscopic techniques, these approaches are often decoupled from measurements under actual operation conditions [9–11]. As a result, the connection between material optimization in the laboratory and performance in application-specific environments remains incomplete. Bridging this gap is essential for the design and reliable deployment of advanced functional materials.

Photocathodes for high-brightness electron sources provide a particularly stringent case for this problem because of the harsh operating conditions of modern photoinjectors. In applications like free-electron lasers (FEL) [12,13], energy-recovery linacs (ERL) [14,15], high-energy physics [16,17], and ultrafast electron diffraction facilities (UED) [18–20], the intrinsic properties of the emitting material set fundamental limits on the beam brightness [5,21]. Material science, therapy, and electron beam lithography for modern chip production are just a few examples that rely on these accelerator-based facilities, making the development of reliable, high-performance photocathodes increasingly important.

Among the wide variety of different photocathodes, semiconducting materials based on bialkali-antimonides are of

[*]Also at Institut für Physik, Humboldt-Universität zu Berlin, 12489 Berlin, Germany.
[†]Also at Institut für Werkstofftechnik, Universität Siegen, 57076 Siegen, Germany.
[‡]Contact author: jonas.dube@helmholtz-berlin.de
[§]Contact author: julius.kuehn@helmholtz-berlin.de

Published by the American Physical Society under the terms of the Creative Commons Attribution 4.0 International license. Further distribution of this work must maintain attribution to the author(s) and the published article's title, journal citation, and DOI.

special interest for high-brightness applications because of their high QE in the visible range and low intrinsic emittance [22]. However, their performance is highly sensitive to chemical composition and contamination, making reproducible preparation and stable operation challenging. Among these materials, Na–K–Sb photocathodes have emerged as promising candidates because of their potential for improved robustness and compatibility with superconducting radio-frequency (SRF) environments. In particular, the absence of cesium (often used for high QE photocathodes) is expected to reduce contamination risks for sensitive superconducting cavities [23]. At the same time, the material system exhibits a narrow window of optimal stoichiometry, and its properties are strongly affected by residual gases and surface modifications. Consequently, reported performance varies significantly, and systematic studies linking material properties to operation under realistic conditions remain scarce [24,25].

In this work, we present a comprehensive study of Na–K–Sb photocathodes that connects controlled synthesis, spectroscopic characterization, intrinsic photoemission properties, and operation in an SRF photoinjector. We establish a growth procedure yielding high QEs of up to 7.5% at 520 nm. The electronic structure and chemical composition of the material were determined using x-ray and ultraviolet photoelectron spectroscopy. The intrinsic photoemission properties are characterized under well-defined laboratory conditions. Finally, we demonstrate operation of the photocathodes in a superconducting RF photoinjector and investigate performance and degradation mechanisms under realistic accelerator conditions for the first time.

By integrating these complementary approaches within a single framework, this work provides a pathway toward a more complete understanding of photoemissive materials across the full chain from synthesis to application. The methodology and insights are transferable to a broader class of functional materials, where linking microscopic properties to device performance remains a central challenge.

II. PHOTOCATHODE PREPARATION

The baseline for the long-time operation of Na–K–Sb photocathodes as electron sources in accelerator is a reproducible growth procedure, but the evaporation of alkali metals, in particular, remains challenging [26,27]. The photocathodes for this study were prepared in the photocathode laboratory at Helmholtz-Zentrum Berlin [28]. The alkali metals are supplied by effusion cells loaded with SAES AlkaMax pills, while antimony (Sb) is evaporated from a thermal cracker cell equipped with Alfa Aesar Sb beads of 99.999% purity. All samples shown in this work were grown on a substrate specially adapted for the use in a superconducting radio-frequency (SRF) photoinjector. It is made from pure molybdenum (Mo) to meet the high requirements of thermal and electric conductivity and has been extensively tested for operation [29–31]. During operation, electric fields up to 30 MV/m may be applied to the cathode with an operating temperature between 80 K and room temperature.

The photocathodes were prepared by a codeposition process of all three materials (triple evaporation) [32]. This method significantly improves the chemical and physical

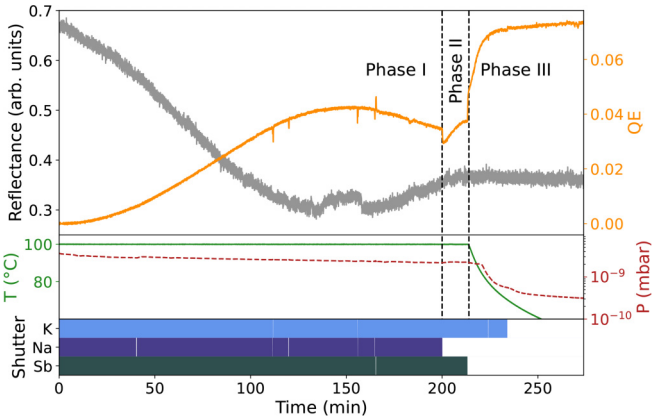


FIG. 1. Growth procedure of TP02. Shown is the development of the QE and reflectance at 520 nm over time (top), the pressure and sample stage temperature (middle), and the shutter states of the three evaporators (bottom). The dark areas in the bottom plot refer to an open shutter state.

roughness of the film, reducing their intrinsic emittance [33]. Before each growth, the deposition rates of the effusion cells are measured with a quartz-crystal microbalance (QCM). An example of the growth sequence is shown in Fig. 1 and consists of a 200 min triple-evaporation phase (phase I), followed by a short K + Sb deposition step for stoichiometry fine-tuning (phase II), and finally a cool-down of the sample with a small residual K flux (phase III). The pressure stays in the low 10^{-9} mbar range during the preparation. In Fig. 1, the reflectance of the sample during the growth is shown. This parameter is a useful tool for the deposition control as it indicates material deposition before first QE can be seen. It is closely related to the QE curve and indicates that a change in QE is often linked to a change in the color of the photocathode. Experiments demonstrated that the K + Sb top layer leads to a reduction of Na on the surface, causing a significant increase in lifetime and having little effect on the final QE [32]. In phase III, the QE is significantly increasing while the photocathode is cooling down. At the beginning of this phase, the K shutter remains open, but the temperature is decreased by 10 °C to reduce the K flux. This avoids desorption of the volatile alkali metals while the sample is still at an elevated temperature. The rather stable reflectance (compared to the strong QE increase) supports the hypothesis that the change in QE is attributable to the temperature change, rather than to continuing K deposition. Further studies are required to fully understand the growth procedure at the crystal level.The shown sample TP02 achieved a QE of 7.5% at 520 nm after the growth, corresponding to the highest QE in the center of the photocathode after all shutters were closed. This QE value is among the highest reported in the literature so far for this material [25,34,35]. The homogeneity of the film was checked by a QE map one day after the growth. As shown in Fig. 2, the deposition system and growth procedure are appropriate for achieving highly homogeneous samples. The majority of the active film has a deviation of less than ±7% relative to the center of the film, while the position with the maximum QE deviates by 10% from the center.

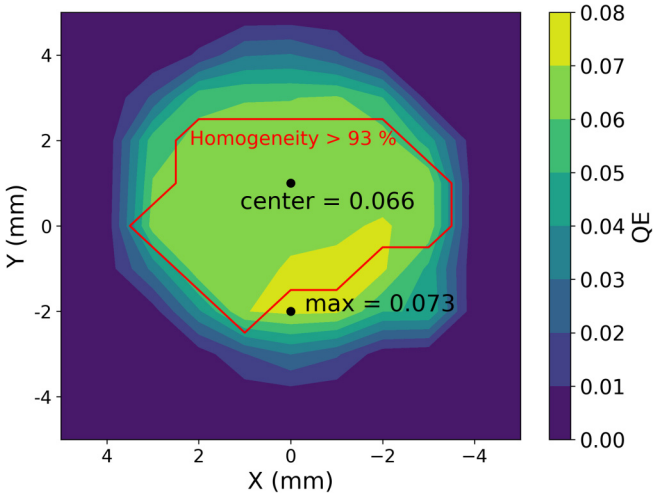


FIG. 2. QE map of the sample TP02 one day after the growth in the preparation system. The center point and the maximum QE are marked. The area of less than ±7% deviation to the center is marked red to show the homogeneity of the film.

In the next sections, the chemical composition and photoemission properties will be characterized and the operational performance will be studied. The photocathodes are highly sensitive to residual gases and are prepared, characterized, operated, and transferred under ultrahighvacuum conditions with a base pressure $<3 \times 10^{-10}$ mbar in all systems, unless otherwise stated. Every transfer of a sample leads to an unavoidable increase in pressure, owing to degassing of moving components such as transfer arms and valves. During all steps of the transfer, the pressure is usually maintained below 1×10^{-9} mbar, but still a degradation of the photocathodes can be observed. Therefore, separate photocathodes were prepared for the different characterization systems and the operation in the SRF photoinjector. An overview of all photocathodes prepared for this work is given in Table I.

III. SPECTROSCOPIC SURFACE ANALYSIS

A. X-ray photoelectron spectroscopy

To determine the chemical composition of the grown Na–K–Sb film, x-ray photoelectron spectroscopy (XPS) measurements were performed on sample SEA00 using an XPS analysis system directly connected to the preparation chamber. All spectra were acquired using nonmonochromatic Al Kα radiation at a power of 250 W and a pass energy of 10 eV. The survey spectrum shown in Fig. 3(a) indicates a high chemical purity of the photocathode, with no detectable contamination peaks. Only a weak Mo 3*d* peak is observed, which is attributed to a signal from an uncoated region of the substrate because of the large spot-size of the x-ray gun.

High-resolution region scans of the Na 1*s* (1087 − 1065 eV), Sb 3*d* (555 − 522 eV) and K 2*p* (311 − 288 eV) core levels were used to calculate the peak areas, as shown in Figs. 3(b)–3(d). Details about the peak fitting and decomposition of the spectra into components are given in the Appendix. The Sb 3*d* spectrum [Fig. 3(c)] exhibits a dominant Sb^{3-} peak with a binding energy of 526.5 eV, and a weak contribution attributed to Sb^0, observed at 528.3 eV. The metallic Sb^0 peak accounts for approximately 6% of the total peak area, indicating that the vast majority of the Sb has fully reacted with the alkali metals. The contribution of the Sb^0 is likely caused by geometric shadowing effects arising from different evaporation angles of the sources and the large spot size of the x-ray gun. The binding energy of the metallic Sb was independently determined by depositing pure Sb on the same substrate, enabling unambiguous identification of the chemical states. The peak at 532.4 eV between the Sb 3*d* doublet, corresponds to the Na KL_1L_{23} Auger peak. No evidence of significant oxidation is observed, as no secondary components are detected in the Na or K spectra.

Relative elemental concentrations were extracted from the peak areas, using the inelastic mean free path, photoionization cross section, and transmission function for each element. The Na Auger peak was not taken into account for the Sb peak area. This analysis yields a chemical composition of $Na_{2.1}K_{1.2}Sb_{1.00}$, close to the theoretically predicted composition of Na_2KSb, previously associated with high QE photocathodes [36]. While absolute concentrations are subject to the typical uncertainties associated with the sensitivity factors and transmission function, relative trends between samples were found to be highly reproducible [32]. With a 95% probing depth of just 4.8 nm for Na, and around 9 nm for K and Sb (calculated by three times the IMFP, sample perpendicular to the analyzer), the final sequential growth steps may have a significant impact on the measured spectra. In particular, the probing depth of Na is smaller than the K + Sb top layer of the photocathode. The still considerable Na concentration indicates its high reactivity and mobility within the film. Therefore, we expect only a small gradient of the Na concentration from the surface to the bulk. The additional K + Sb layer stabilizes the surface composition and significantly increases the lifetime by reacting with excess Na.

TABLE I. Overview of the photocathodes discussed in this work. If no lifetime is given, the QE was not decreasing but still increasing during the duration of the lifetime measurement.

Sample ID	QE (%) after Growth	Lifetime (h)	Purpose	Details in Sec.
TP02	7.5	336	PhoTEx	IV
TWH30	3.8		UPS	III
SEA00	5.0	211	XPS	III
SEA01	4.2		SEALab	V
SEA02	3.6	108	SEALab	V
SEA03	5.5	989	SEALab	V

B. Ultraviolet photoelectron spectroscopy

Besides the chemical composition, the work function is a key parameter of the material, especially as it is directly linked to the photoemissive threshold energy, which describes QE and MTE. For metals, the work function Φ and threshold energy E_T are equal and defined by the difference between the vacuum level and the Fermi level E_F. However, for semiconductors, the threshold energy is given by the energy difference between the vacuum level and the valence band

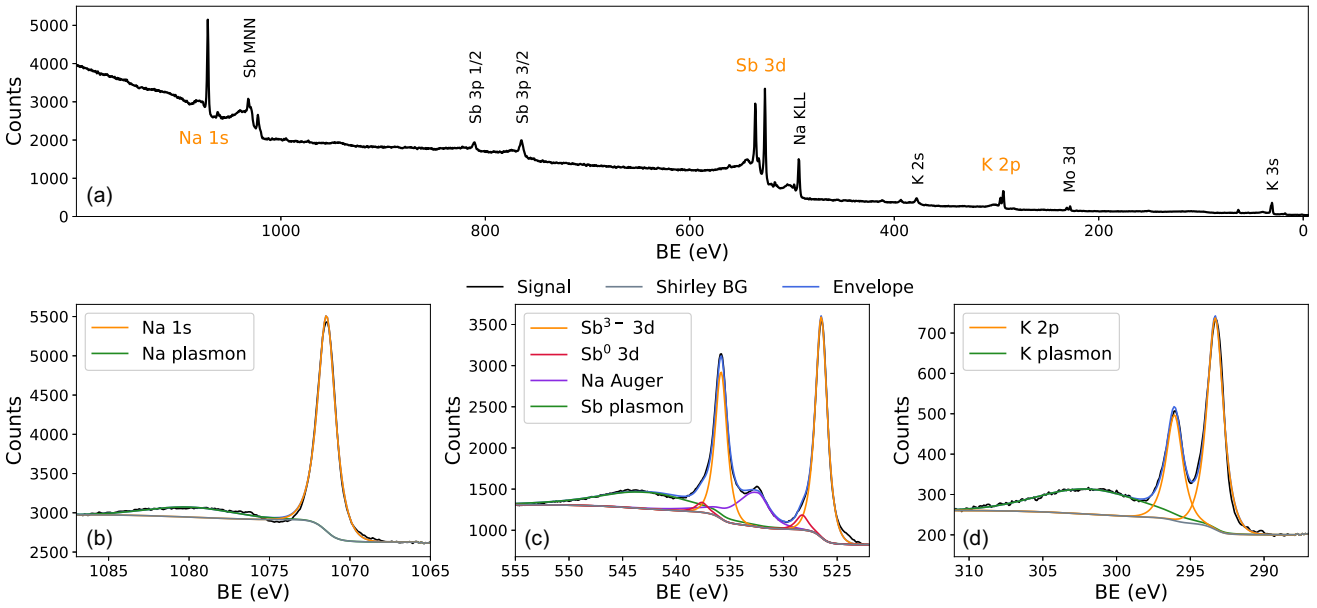


FIG. 3. XPS measurements of the Na–K–Sb photocathode SEA00. (a) Survey spectrum; region scans of (b) Na 1*s*, (c) Sb 3*d*, (d) K 2*p* core levels used for quantification. The data was fitted for peak separation after background subtraction (Shirley BG). The fitting parameters and more details are given in Appendix.

maximum (VBM),

$$E_T = \Phi + (E_F - \mathrm{VBM}). \tag{1}$$

The photocathode TWH30 was transferred to an off-synchrotron spectroscopy system in the EMIL laboratory [37] to measure the secondary electron cutoff (SECO) by ultraviolet photoelectron spectroscopy (UPS) [38,39]. The measurement was performed 10 days after growth, and the photocathode had a remaining QE of 1.3% in the suitcase just before it was moved to the UPS system. It is likely that the photocathode further degraded owing to the higher base pressure of 2×10^{-9} mbar in this system.

A He I source with an excitation energy of 21.2 eV was used for the UPS measurements and the samples were biased with 10 V. The energy scale was set by defining the kinetic energy of the Fermi-edge electrons as the maximum available energy of 21.2 eV [39]. Since the Fermi energy of a semiconductor cannot be measured directly, the Fermi edge of gold (Au) was measured for calibration, as shown in Fig. 4. This is possible, since all Fermi edges align to the same value, as they are electrically connected. In Fig. 4, the SECO of the photocathode is shown, and the onset of electron emission is determined by linear fits. After subtracting the bias voltage of 10 V, the work function can be determined to be $\Phi = 1.81$ eV. To determine the threshold energy, also the distance of the VBM to the Fermi edge was measured to be 0.40 eV, resulting in a threshold energy of $E_T = 2.21$ eV. This parameter is highly sensitive to contaminants on the photocathode surface, which increase the work function and threshold energy. As the sample TWH30 has already been degraded at the time of the measurement, these values might be smaller for a less degraded photocathode, which is also indicated by the flattened onset of the SECO. In earlier studies the threshold energy of Na–K–Sb photocathodes was reported to be 2.0 eV and 2.1 eV for Cs–K–Sb [21,40]. This is in very good agreement with our measurements.

IV. PHOTOEMISSION CHARACTERIZATION

With the chemical state and threshold energy of the photocathode well characterized, we now turn to the intrinsic photoemission properties that determine brightness and beam quality. Both the QE and MTE are dependent on the threshold energy E_T of the material and the energy of the illuminating photons $\hbar\omega$. High electric fields reduce the barrier between the material and the vacuum, a phenomenon known as the Schottky effect [41]. In a first approximation, the QE is then

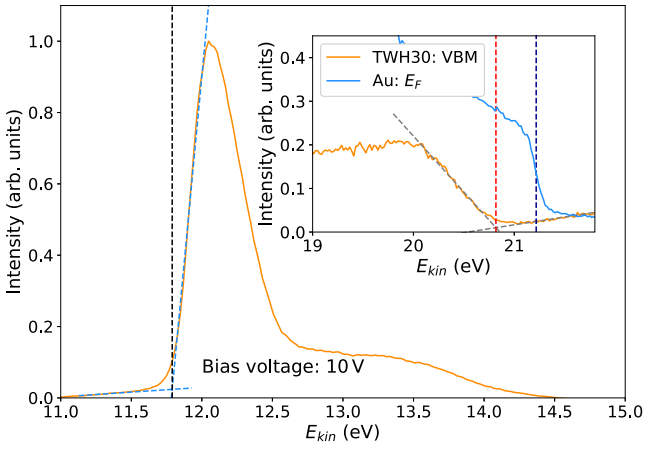


FIG. 4. Secondary electron cutoff for the sample TWH30, measured with UPS. In the subfigure, the valence band maximum (VBM) of the photocathode is shown, as well as the Fermi edge of Au for calibration.

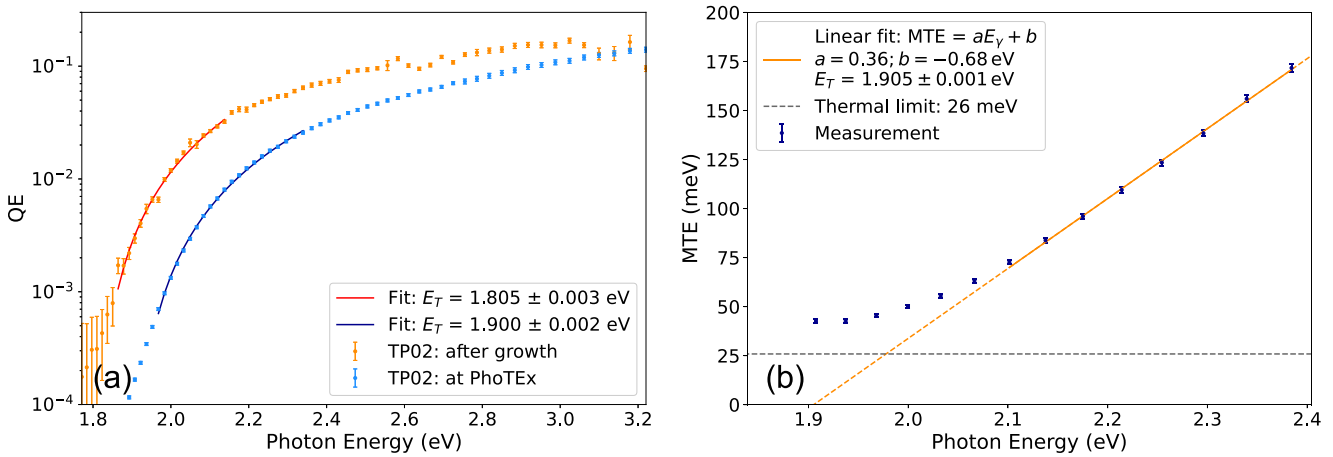


FIG. 5. Characterization of the photoemission properties of photocathode TP02 at PhoTEx. (a) Spectral response curve of TP02 after growth (orange) and after the transfer to PhoTEx (blue). (b) MTE as a function of the photon energy for TP02 showing an MTE of 172 ± 2 meV at 520 nm. The fit range is indicated by a solid line.

given by

$$\mathrm{QE} \propto \left(\hbar\omega - E_T + \sqrt{\frac{e^3}{4\pi\epsilon_0}E\sin\Theta}\right)^2, \tag{2}$$

with E the electric field at the photocathode surface, Θ the RF phase, e the electric charge, and ϵ_0 the vacuum permittivity. The MTE is given by

$$\mathrm{MTE} = \frac{\hbar\omega - E_T}{3}, \tag{3}$$

assuming low fields, and therefore a negligible Schottky effect in this case.

The threshold energy of the photocathode might change over time, for example owing to oxygen on the surface. It is therefore a suitable parameter to describe the aging of the material, as it has a direct influence to the photocathode performance. It can be determined by measuring the QE or MTE at different photon energies or field strengths. While the QE can easily be measured in most deposition systems, the measurement of the MTE requires a setup for low-energy electron spectroscopy in the meV range. We developed the Photoemission and Transverse Energy Experiment (PhoTEx), which allows the spectrally resolved measurement of QE, MTE, reflectance, and color under well-defined laboratory conditions [28]. Equipped with a microchannel plate, the setup has a high sensitivity, which allows the illumination of the photocathode with very low light intensity, to avoid space charge effects. The photocathode TP02 with an initial QE of 7.5% has been transferred to PhoTEx with a remaining QE of 3.1% upon arrival at PhoTEx. So far, this is the highest QE measured after transfer to a different vacuum system.

The spectral response of the photocathode has been measured before and after the transfer and is shown in Fig. 5(a). It is evident that the degradation of the QE is accompanied by a shift in the threshold energy. Using Eq. (2), the change can be quantified by fitting the QE close to the emission threshold, with the Schottky term being neglected in this instance. After the transfer, E_T has increased by 0.095 eV from 1.805 to 1.900 eV. The MTE has been measured for different wavelengths directly after the spectral response and is shown in Fig. 5(b). For different photon energies well above the threshold, the MTE increases linearly and can be fitted by Eq. (3), yielding a slope close to the theoretically predicted value of 1/3. Close to the threshold, however, the MTE saturates at 43 meV, which is approximately 17 meV above the thermal limit. This offset is attributed to chemical roughness of the film, i.e., local variations of the surface potential. Gevorkyan *et al.* [33] demonstrated, that even small rms surface-potential variations of 10 mV can result in an MTE increase on the order of tens of meV. The comparatively small MTE observed for TP02 indicates that the potential fluctuations are very small for our photocathodes, thereby supporting the high chemical uniformity of the triple-evaporation procedure. Additional contributions from physical roughness may occur, but are only observed at higher electric fields [33]. From the fit parameters, the threshold energy can be determined to be $E_T = (1.905 \pm 0.001)$ eV, which is in close agreement with the value calculated from the spectral-response fit. At 520 nm, an MTE of 172 ± 2 meV was measured. This value is comparable to the MTE of Cs–K–Sb photocathodes, measured to be 160 meV at 532 nm [42].

V. OPERATIONAL EXPERIENCE

After the characterization in a well-defined laboratory environment, we will now focus on the performance of the photocathodes under real accelerator conditions. The photocathodes SEA01, SEA02, and SEA03 have been used for the commissioning of the SRF photoinjector at the *Sustainable Electron Accelerator Laboratory* (SEALab, formerly bERLinPro) [15,43,44], demonstrating the operation of an SRF photoinjector with a sodium-based photocathode for the first time. The photoinjector was designed to achieve a low emittance of 1 μm rad at 77 pC bunch charge, an average current of 100 mA and beam energies up to 2.5 MeV. For the commissioning of all systems, the photoinjector has been operated at much lower bunch charges, up to 3.5 pC, and fields reaching 16 MV/m. The photocathode was retracted

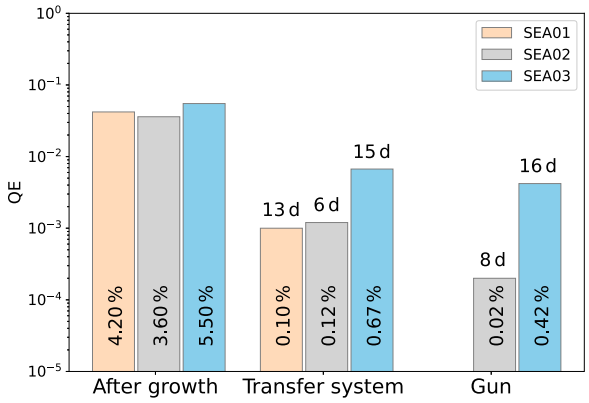


FIG. 6. Overview of all photocathodes prepared for the photoinjector of SEALab. Shown are the QE values after the growth, in the transfer system at the photoinjector and inserted into the gun. On top of the bars, also the elapsed days after the growth are given.

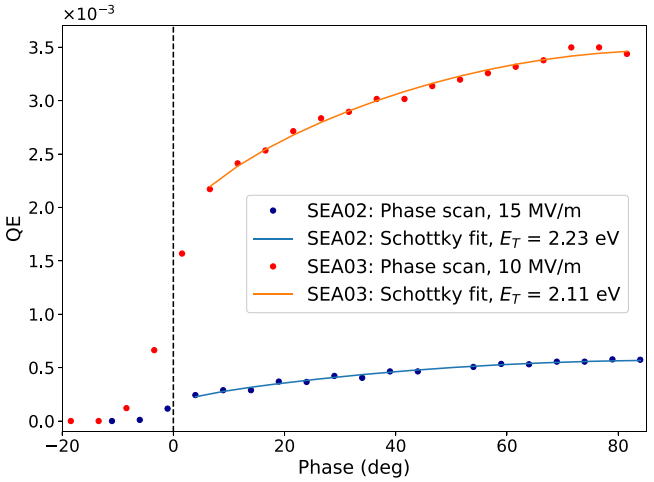


FIG. 7. Schottky scans of photocathodes SEA02 and SEA03 in the SRF photoinjector of SEALab. The threshold energy is determined by fitting the data with Eq. (2), showing an increase for SEA02.

by 2 mm during commissioning, to avoid the thermal load from the RF. The 522 nm drive laser has been operated at a frequency of 1 MHz and a pulse length of 4 ps (FWHM). In this section, we will focus on the parameters related to the photocathode. Beam-related analysis will be part of a second paper by Brookes and colleagues.

The photocathodes are transferred from the photocathode laboratory to the photoinjector, using a compact vacuum suitcase with a base pressure of $<3 \times 10^{-11}$ mbar. A transfer system is attached to each of the systems to load and unload the suitcase [29]. During the last step of the transfer, the photocathode is moved from the transfer system to the backwall of the cavity while cooling down from room temperature to 80 K. All systems used for photocathode preparation and transfer are set up under clean room conditions to avoid particulate contamination during the process, which might impede the cavity performance. Until end of 2025, three photocathodes have been prepared for SEALab. An overview of the photocathodes is given in Fig. 6, showing the QE after the growth, in the transfer system at the photoinjector, and after insertion into the gun. On top of each bar, the number of days after growth is shown. The photocathode SEA01 could not be operated in the injector, because of a malfunction of the RF power coupler, but the QE had already degraded by more than one order of magnitude from the preparation system to the transfer system. SEA02 lost about two orders of magnitude from the preparation system to the gun. Afterwards, optimizations to the vacuum systems were made to improve the pressure during the transfer. Additionally, a significantly longer lifetime has been achieved for the photocathode SEA03. The photocathode had a remaining QE of 0.42%, even after additional unwanted gas exposure in the transfer system and delayed insertion owing to a malfunctioning transfer mechanism. The photocathode SEA02 has been operated for six weeks in the photoinjector, while SEA03 has been operated for 11 days, before the run was interrupted by a power failure that caused a warm-up of the photoinjector. Both photocathodes were thoroughly tested, to determine their performance and operational lifetime.

A. Compatibility with the SRF Environment

The integration of alkali-antimonide photocathodes into the SRF photoinjector environment poses several challenges, including multipacting, field emission, and contamination risks. Therefore, they are one of the main performance criteria for the photocathode. During the first tests of SEA02, one multipacting event occurred, which could be suppressed by applying a bias voltage of −3 kV DC to the photocathode. Later, the same bias voltage has been applied every time the photoinjector was operated, and no further multipacting events have been observed. Field emission has been observed for both photocathodes at field levels higher than 10 MV/m, which is also the field emission onset for the empty cavity without a photocathode plug inserted. Therefore, any possible contributions from the photocathode are expected to be small. Both multipacting and field emission indicate good compatibility between the Na–K–Sb photocathode and the sensitive SRF environment.

B. Thermal emittance

The photoemission characterization in Sec. III B revealed a good agreement of the QE and MTE with theoretical models. In particular, the threshold energy was identified as a key parameter to describe the photoemission properties. The primary objective of this section is to investigate whether the intrinsic photoemission properties remain predictive under realistic operating conditions. At SEALab, the threshold energy was measured by performing Schottky scans as shown in Fig. 7. The launch phase between the laser and the RF was varied, while the QE was measured via the drain current of the photocathode and fitted with Eq. (2). The measured threshold energies significantly differ and correlate with their degradation state observed in the QE. With QE = 0.42%, the threshold energy of SEA03, $E_T = 2.11$ eV, is slightly increased compared to that of the sample TP02, investigated at PhoTEx. SEA02 was even more degraded and reached a significantly larger value of $E_T = 2.23$ eV, in line with its low

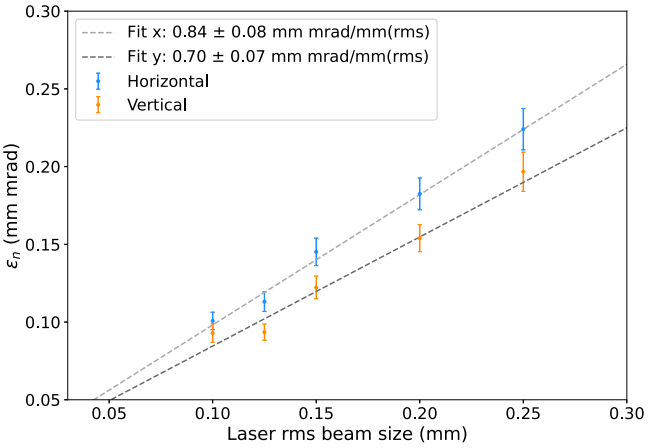


FIG. 8. Normalized emittance measured for different laser spot sizes for photocathode SEA03 at 10 MV/m.

remaining QE. With a threshold energy of $E_T = 2.11$ eV for SEA03, the expected MTE would be MTE ≈ 90 meV. The Schottky effect will increase this value through a reduction in the effective work function, resulting in an expected MTE of 130 meV at a field of 10 MV/m. To verify this value, the normalized emittance of SEA03 was measured for different laser-spot sizes at this field, using solenoid scans, as shown in Fig. 8. The superconducting solenoid is located directly behind the cavity. The emittance was determined by measuring the electron beam size at a fluorescence screen for different solenoid strengths. The geometric emittance was calculated from the known beam-transfer matrices and normalized with the beam energy. From this data, the intrinsic emittance of the photocathode (MTE) can be determined using

$$\varepsilon_{x,y} = \sigma_{x,y}\sqrt{\frac{\mathrm{MTE}}{mc^2}}, \tag{4}$$

with $\sigma_{x,y}$ being the rms laser spot size, m the electron mass, and c the speed of light in vacuum [42]. This equation assumes no additional emittance sources from cavity or beam transport. We only considered data points down to an rms beam size of 0.1 mm, as we observed diffraction of the laser for smaller apertures. In Fig. 8, an offset between the x and y axes can be seen, with a horizontal emittance of $\varepsilon_x = 0.84 \pm 0.08$ mm mrad/mm and a vertical emittance of $\varepsilon_y = 0.70 \pm 0.07$ mm mrad/mm. This would correspond to MTE values of 359 ± 68 meV and 251 ± 54 meV, respectively. This indicates that the MTE increased by a factor of 2 in the y direction during beam transport, while the MTE in the x direction is about 2.8 times larger than the expected value. Since the photocathode showed good agreement with theoretical models in the laboratory, we do not expect that this effect to be caused by the photocathode but rather by additional emittance contributions arising from aberrations in the solenoid and distortions of the RF field.

C. Degradation and operational lifetime

For a stable long-term operation of Na–K–Sb photocathodes in an accelerator, it is necessary to observe and understand the degradation mechanisms of this material. To investigate the degradation in the photoinjector, the photocathode QE has been regularly tracked and was measured by the drain current with a constant bias voltage of -5 kV applied to the photocathode. The RF field was turned off during these measurements. In Fig. 9, the development of the QE of SEA02 in the photoinjector is shown together with the operation time of the RF. In addition to the overall trend, we discuss a few events in more detail.

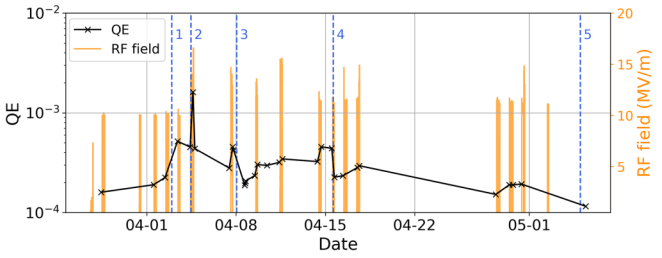


FIG. 9. Development of the QE of SEA02 during 6 weeks of operation. Few important events are marked: (1) and (2) QE enhancement during beam operation; (3) cryo and vacuum incident; (4) change in laser position; (5) start warm up of gun.

At the events (1) and (2) a significant increase of the QE occurred during beam operation. After the first event, the QE remained at a high level. At the second event, the increase was only observed directly after the operation and had fallen back to its original value one day later. During this event, the photoinjector was operated at fields up to 16 MV/m and the QE increased by more than a factor of 6. Because of the low laser power and field strength, photocathode heating can be disregarded as a potential factor. The increase stopped, when the laser shutter was closed and only occurred with RF and laser in operation, indicating a beam related effect. Similar behavior has previously been observed for Cs–K–Sb photocathodes [45], but the mechanism is not yet fully understood. QE maps were taken before and after the operation on that day. They revealed that in this case the QE rejuvenation was a global effect and not limited to the extraction point, as shown in Fig. 10.

A severe vacuum and cryogenic incident happened at event (3), with a pressure of 1×10^{-8} mbar detected for about

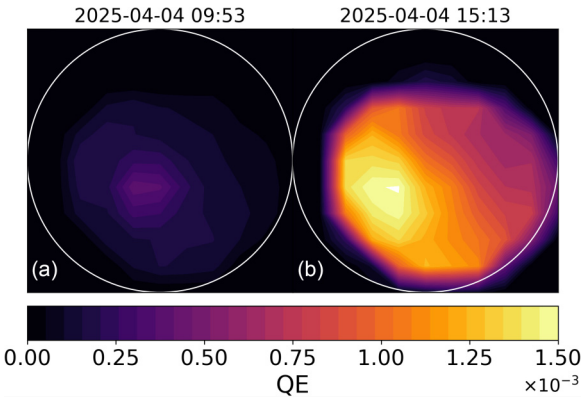


FIG. 10. QE maps of SEA02 showing a QE rejuvenation after one day of beam operation at 16 MV/m. The white circles mark the edges of the photocathode plug with 10 mm diameter. (a) Before operation; (b) after operation at the event (2) in Fig. 9.

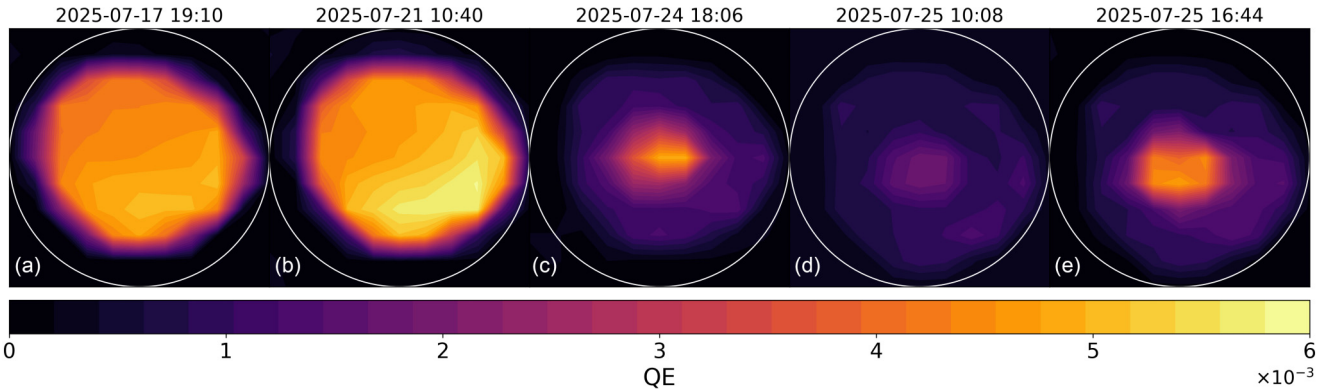


FIG. 11. QE maps of SEA03 showing significant changes in the QE distribution. The white circles mark the edges of the photocathode plug with 10 mm diameter. (a) directly after transfer; (b) recovered from transfer; (c)–(e) degradation and recovery after a 360 deg phase scan.

30 minutes at the front of the photoinjector. As the gauge is more than 1 m away, the actual gas exposure to the photocathode is unknown, but a significant reduction of the QE was observed. During the next days, the photocathode fully recovered and returned to the value before the incident. Recovery was observed with and without beam operation, but the QE increased significantly faster during operation. The QE jump at event (4) was not caused by degradation of the photocathode, but by a change in the laser position to adjust the beam to the electrical center of the cavity. Therefore, the laser had to be moved to a position with less QE. The final annotation in Fig. 9 marks the beginning of the warm-up of the photoinjector. Overall, it can be noted, that no significant reduction of the QE was observed after six weeks.

While most theoretical models of the degradation process only describe the reduction of the QE, Pavlenko *et al.* [46] use a kinetic model that is able to also describe a recovery process. The adsorbed species initially occupy a weakly bound, metastable state before transitioning to an irreversible chemically bound state. If desorption occurs before permanent bonding, the photocathode can recover. This behavior was observed after the vacuum incident at event (3). The photocathode SEA02 was already significantly degraded directly after insertion into the photoinjector. Therefore, a large fraction of reactive surface sites was likely occupied by contaminants, which may slow down permanent chemical bonding, while weak adsorption states increase. This surface saturation could explain the complete recovery after the vacuum incident. The accelerated recovery during beam operation indicates that beam-induced effects, such as electron emission stimulated desorption, may enhance this process. This effect could therefore also be responsible for the significant QE increase at events (1) and (2). A quantitative investigation of beam-assisted desorption will be required to fully understand this behavior.

D. Electron back bombardment

The photocathode SEA03 could only be operated for 11 days, before a power failure caused the cryomodule to warm up, but interesting developments of the QE could be observed during the operation period, as shown in Fig. 11. The QE map in subfigure (a) was measured directly after the photocathode insertion into the photoinjector. The photocathode homogeneously recovered from the increased pressure during the transfer (b). On April 24, a full 360° scan of the launch phase at a field strength of 9.5 MV/m was performed. Severe damage to the photocathode was observed afterwards. The QE map in Fig. 11(c) was taken immediately after the scan; however, the QE continued to decrease overnight, without further operation. After one day of normal operation, the QE partially recovered to the state shown in Fig. 11(e). A similar ring-shaped degradation has also been observed for Cs–K–Sb photocathodes during operation in an RF gun [47], although the underlying mechanism has remained unclear. During the phase scan, the photoinjector was operated at launch phases with a majority of the electrons not leaving the photoinjector, but being back-accelerated onto the back-wall of the cavity and the photocathode. These electron-back-bombardment (EBB) events are therefore a likely origin of the observed local damage. To further investigate the mechanism, particle tracking simulations of the 360° phase scan were performed.

The simulations were performed using CST Studio Suite [48] based on the electromagnetic field distributions of the SRF gun derived from the x-ray tomography model of the cavity [49]. The simulations reproduced the experimental conditions during the phase scan, including the field level, pulse length, bunch charge, space-charge effects, and the applied −3 kV DC bias at the photocathode. A total of 9.9×10^5 macroparticles from 3.9×10^4 emission points were tracked through a simulated domain of 555 mm discretized with 10.2×10^6 hexahedral mesh cells. A 2D monitor placed in the photocathode plane recorded the impact position and momentum of each particle returning to the photocathode surface. The strongest interaction was observed at a launch phase of 82°, as shown in Figs. 12(a) and 12(c). At this phase, electrons with kinetic energies up to $E_{\mathrm{kin}} = 0.45$ MeV struck over nearly the entire photocathode, with the highest particle density in the center of the film. In contrast, at other phases [e.g., 140°, as shown in Figs. 12(b) and 12(d)], the returning electrons exhibit significantly lower kinetic energies and are confined to the central 3 mm of the photocathode.

Experimentally, the degradation manifests as a ring-shaped structure surrounding the center. This indicates that localized damage is not determined by the total number of returning

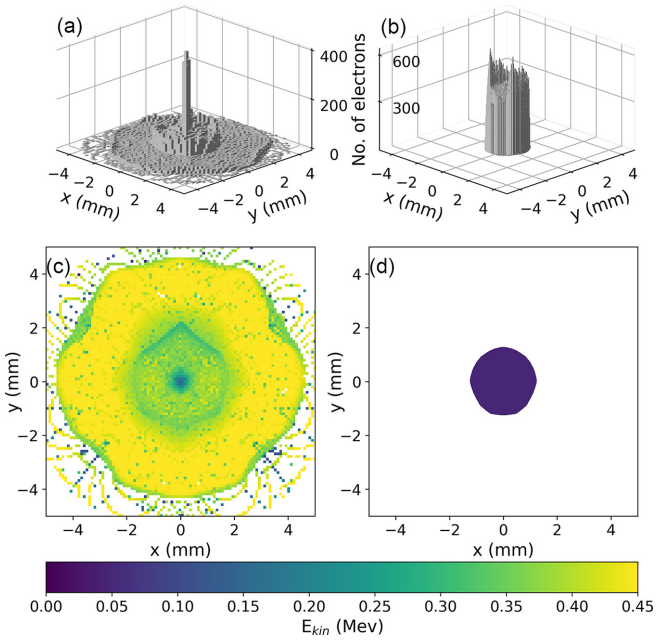


FIG. 12. Particle tracking simulations of electron back bombardment on the photocathode during a phase scan. (a) electron distribution at 82°; (b) electron distribution at 140°; (c), (d) mean kinetic energy per bin for 82° and 140°, respectively.

electrons, but rather by their impact energy. In particular, the simulations suggest that a comparatively small fraction of highenergy electrons at a phase of 82° can induce severe damage to the photocathode.

Interestingly, the central region exhibits less pronounced degradation, despite experiencing the most high-energy particles and an even larger flux of low-energy electrons (<50 keV). Two possible explanations may account for this behavior: (i) continuous photoemission in the extraction region may have a stabilizing effect, or (ii) low-energy electrons may induce partial surface recovery via electron-stimulated desorption or local chemical reordering. While the exact microscopic mechanism requires further investigation, the observations clearly indicate that electrons with kinetic energies below <50 keV have a negligible contribution to irreversible degradation under the present conditions. The total deposited power from EBB is below 1 μW, excluding any thermal contributions to degradation or rejuvenation.

VI. CONCLUSIONS

In this work, we established a comprehensive framework for the development and evaluation of photoemissive materials by quantitatively linking synthesis, electronic structure, intrinsic photoemission properties, and operational performance. A unique molybdenum-based plug system enables the direct transfer between preparation, detailed characterization, and insertion into the SRF photoinjector, providing a harsh test environment.

The developed growth procedure shows good agreement between the experimental results and theoretical models, achieving a QE of up to 7.5% and an MTE of 172 meV at 520 nm. A high chemical purity of the film was confirmed by *in situ* photoelectron spectroscopy. By combining ultraviolet photoelectron spectroscopy, spectral response measurements, intrinsic emittance analysis, and Schottky scans, the photoemission threshold energy was identified as a unifying parameter that directly connects surface chemistry to emission properties and is accessible in most setups. Its systematic evolution with degradation establishes a quantitative metric that consistently correlates with both QE and MTE across different experimental platforms.

Operation in a superconducting radio-frequency photoinjector demonstrates the transferability of these materials to realistic operational conditions. Operation over several weeks, together with the absence of enhanced field emission or multipacting, confirms the high compatibility between the Na–K–Sb photocathode and the sensitive SRF cavity. The photocathode was operated for six weeks without a significant loss in QE. The accelerated recovery during beam operation suggests electron-induced desorption of weakly bound contaminants from the photocathode surface, demonstrating the robustness of the system. The combination of experiments and particle tracking simulations identifies electron-back bombardment and surface adsorption processes as the dominant mechanisms of sample degradation. In particular, high-energy electrons with energies >0.4 MeV are found to drive irreversible damage, while low-energy electrons ($E_{\mathrm{kin}} < 50$ keV) striking the photocathode surface have no negative effect on the photocathode performance and may even contribute to surface recovery.

Together, these results establish a quantitative framework that bridges material synthesis, electronic structure, and the operational performance of bialkali-antimonide photocathodes. More generally, the successful deployment of photoemissive materials follows a sequence of tightly coupled steps. A stable and reproducible growth procedure forms the foundation, ideally supported by immediate feedback on the QE for process optimization. Complementary XPS measurements enable access to the electronic structure and chemical composition, thereby guiding the improvement of the preparation process. While advanced methods such as UPS offer deeper insights into the emission threshold, they are usually not required for routine optimization.

As device complexity increases, distinguishing between intrinsic material properties and contributions from the machine becomes increasingly challenging. Especially when the performance of the photocathode is highly critical for operation, measurements of the photoemission properties under well-defined laboratory conditions are essential to establish reliable performance metrics. Ultimately, a validation under realistic operating conditions is crucial to assess stability, degradation mechanisms, and long-term performance. Bridging these stages remains challenging, as the transfer of highly sensitive materials under ultra-high vacuum conditions continues to limit reproducibility and performance.

The framework presented in this work provides a general pathway to systematically connect these steps, enabling the development and integration of advanced photoemissive materials across a broad range of scientific and technological applications.

TABLE II. XPS fitting parameters.

Component	Line shape	Position	FWHM	Area
Na 1*s*	GL(80)	1071.45	1.29	4235.1
Na plasmon	GL(0)	1079.94	6.30	853.23
Sb^{3-} 3*d* 5/2	GL(80)	526.48	1.31	4194.9
Sb3− 3*d* 3/2	GL(80)	535.82	1.31	2796.6
Sb^0 3*d* 5/2	GL(80)	528.26	1.31	283.5
Sb^0 3*d* 3/2	GL(80)	537.60	1.31	188.97
Na auger	GL(80)T(1)	532.44	2.59	1913.59
Sb plasmon	GL(80)T(3)	542.54	9.36	2363.56
K 2*p* 3/2	GL(80)	293.30	1.31	818.91
K 2*p* 1/2	GL(80)	296.07	1.31	409.46
K plasmon	GL(0)	301.8	8.35	553.55

ACKNOWLEDGMENTS

The authors thank Alice Galdi for the help during the UPS measurements, the scientific exchange, and valuable discussions. The authors thank Michael Schuster and André Frahm for their help with the photocathode transfer at SEALab, Jan Ullrich for the assembly of the vacuum suitcase, Malte Gotz for control systems, and Günther Rehm for diagnostics. The authors acknowledge the help of Regan Wilks, Wolfgang Bremsteller, and Johannes Frisch during the UPS measurements at the EMIL/SISSY laboratory. This work was funded by the Deutsche Forschungsgemeinschaft (DFG) - Project No. 490940284, the German Bundesministerium für Forschung, Technologie und Raumfahrt, Land Berlin and grants of the Helmholtz Association.

J.D. conceived the project; curated the data; performed the formal analysis and investigation; prepared the visualizations; wrote the original draft; and participated in reviewing and editing the manuscript. C.W. contributed to data curation, formal analysis, and resources. E.J.B. contributed to the investigation, resources, validation, and review and editing of the manuscript. A.N. contributed to the formal analysis and investigation, administered the project, and participated in reviewing and editing the manuscript. G.K. contributed to the investigation, resources, and review and editing of the manuscript. E.E. contributed to the investigation and resources. P.E. contributed resources and participated in reviewing and editing the manuscript. A.U. contributed resources. T.K. acquired funding, administered the project, supervised the work, and participated in reviewing and editing the manuscript. J.K. contributed to the project conceptualization, data curation, formal analysis, investigation, project administration, resources, supervision, preparation of the original draft, and review and editing of the manuscript.

DATA AVAILABILITY

The data that support the findings of this article are not publicly available upon publication because it is not technically feasible and/or the cost of preparing, depositing, and hosting the data would be prohibitive within the terms of this research project. The data are available from the authors upon reasonable request.

APPENDIX: XPS FITTING PARAMETERS

The fitting of the XPS data in Fig. 3 has been performed with CasaXPS [50]. A Shirley background was subtracted from the data. Doublet peaks were fitted using a fixed peak separation and fixed full width at half maximum (FWHM). Area constraints were applied with a ratio of 6:4 for *d* orbitals and 8:6 for *p* orbitals. A Gaussian/Lorentzian product formula with a mixing coefficient of $m = 80$ was used for all main peaks, with $m = 0$ corresponding to a pure Gaussian and $m = 1$ being a pure Lorentzian. A pure Gaussian line shape was used for the Na and K plasmon peaks. An exponential blend function $T(k)$ was applied to the Na Auger peak and the Sb plasmon. All details about the line shapes and the fitting results are given in Table II.

[1] G. Zeng, T. A. Pham, S. Vanka, G. Liu, C. Song, J. K. Cooper, Z. Mi, T. Ogitsu, and F. M. Toma, Development of a photoelectrochemically self-improving Si/GaN photocathode for efficient and durable H_2 production, Nat. Mater. **20**, 1130 (2021).

[2] K. Nakamura, Y. Hamana, Y. Ishigami, and T. Matsui, Latest bialkali photocathode with ultra high sensitivity, Nucl. Instrum. Methods Phys. Res. Sec. A **623**, 276 (2010).

[3] R. Marchand, R. Šachl, M. Kalbáč, M. Hof, R. Tromp, M. Amaro, S. J. van der Molen, and T. Juffmann, Optical near-field electron microscopy, Phys. Rev. Appl. **16**, 014008 (2021).

[4] V. N. Litvinenko, N. Bachhawat, J. C. Brutus, L. Cultrera, K. Decker, M. Gaowei, P. Inacker, Y. Jing, J. Ma, K. P. Mondal, *et al.*, Towards advanced polarized electron sources, Nat. Phys. **22**, 325 (2026).

[5] I. V. Bazarov, B. M. Dunham, and C. K. Sinclair, Maximum achievable beam brightness from photoinjectors, Phys. Rev. Lett. **102**, 104801 (2009).

[6] P. Musumeci, J. Giner Navarro, J. B. Rosenzweig, L. Cultrera, I. Bazarov, J. Maxson, S. Karkare, and H. Padmore, Advances in bright electron sources, Nucl. Instrum. Methods Phys. Res. Sec. A **907**, 209 (2018).

[7] C. T. Parzyck, C. A. Pennington, W. J. I. DeBenedetti, J. Balajka, E. M. Echeverria, H. Paik, L. Moreschini, B. D. Faeth, C. Hu, J. K. Nangoi, *et al.*, Atomically smooth films of CsSb: A chemically robust visible light photocathode, APL Mater. **11**, 101125 (2023).

[8] L. Guo, K. Shiohara, H. Yamaguchi, G. Wang, Y. Okabe, M. Nakatake, S. Takakura, M. Yamamoto, S. Ogawa, and Y. Takashima, Improved robustness of sequentially deposited potassium cesium antimonide photocathodes achieved by increasing the potassium content towards theoretical stoichiometry, Sci. Rep. **15**, 2900 (2025).

[9] V. Pavlenko, J. Smedley, A. Scheinker, R. L. Fleming, A. Alexander, M. A. Hoffbauer, and N. A. Moody, Stoichiometry control and automated growth of alkali antimonide photocathode films by molecular beam deposition, Appl. Phys. Lett. **120**, 091901 (2022).

[10] C. A. Pennington, M. Gaowei, E. M. Echeverria, K. Evans-Lutterodt, A. Galdi, T. Juffmann, S. Karkare, J. Maxson,

S. J. van der Molen, P. Saha, J. Smedley, W. G. Stam, and R. M. Tromp, A structural analysis of ordered Cs_3Sb films grown on single crystal graphene and silicon carbide substrates, APL Mater. **13**, 011120 (2025).

[11] W. G. Stam, M. Gaowei, E. M. Echeverria, K. Evans-Lutterodt, J. Jordan-Sweet, T. Juffmann, S. Karkare, J. Maxson, S. J. van der Molen, C. Pennington, P. Saha, J. Smedley, and R. M. Tromp, Growth of ultra-flat ultra-thin alkali antimonide photocathode films, APL Mater. **12**, 061114 (2024).

[12] P. Emma, R. Akre, J. Arthur, R. Bionta, C. Bostedt, J. Bozek, A. Brachmann, P. Bucksbaum, R. Coffee, F.-J. Decker, *et al.*, First lasing and operation of an ångstrom-wavelength free-electron laser, Nat. Photon. **4**, 641 (2010).

[13] R. Xiang, A. Arnold, and J. W. Lewellen, Superconducting radio frequency photoinjectors for CW-XFEL, Front. Phys. **11**, 1166179 (2023).

[14] Z. T. Zhao, Z. Wang, C. Feng, S. Chen, and L. Cao, Energy recovery linac based fully coherent light source, Sci. Rep. **11**, 23875 (2021).

[15] A. Neumann, B. Alberdi, T. Birke, P. Echevarria, D. Eichel, F. Falkenstern, R. Fleischhauer, A. Frahm, F. Goebel, A. Heugel, *et al.*, bERLinPro becomes SEALab: Status and perspective of the energy recovery linac at HZB, in *Proceedings of 13th International Particle Accelerator Conference, Bangkok, Thailand, Jun. 2022* (JACoW Publishing, Geneva, Switzerland, 2022), pp. 1110–1113.

[16] V. Rusetsky, V. Golyashov, S. Eremeev, D. Kustov, I. Rusinov, T. Shamirzaev, A. Mironov, A. Demin, and O. Tereshchenko, New spin-polarized electron source based on alkali antimonide photocathode, Phys. Rev. Lett. **129**, 166802 (2022).

[17] J. Schaber, R. Xiang, and N. Gaponik, Review of photocathodes for electron beam sources in particle accelerators, J. Mater. Chem. C **11**, 3162 (2023).

[18] D. Filippetto, P. Musumeci, R. Li, B. Siwick, M. Otto, M. Centurion, and J. Nunes, Ultrafast electron diffraction: Visualizing dynamic states of matter, Rev. Mod. Phys. **94**, 045004 (2022).

[19] A. H. Zewail, 4D Ultrafast electron diffraction, crystallography, and microscopy, Annu. Rev. Phys. Chem. **57**, 65 (2006).

[20] B. Alberdi Esuain, J.-G. Hwang, A. Neumann, and T. Kamps, Novel approach to push the limit of temporal resolution in ultrafast electron diffraction accelerators, Sci. Rep. **12**, 13365 (2022).

[21] D. H. Dowell, I. Bazarov, B. Dunham, K. Harkay, C. Hernandez-Garcia, R. Legg, H. Padmore, T. Rao, J. Smedley, and W. Wan, Cathode R&D for future light sources, Nucl. Instrum. Methods Phys. Res. Sec. A **622**, 685 (2010).

[22] I. Petrushina, V. Litvinenko, Y. Jing, J. Ma, I. Pinayev, K. Shih, G. Wang, Y. Wu, Z. Altinbas, J. Brutus, *et al.*, High-brightness continuous-wave electron beams from superconducting radio-frequency photoemission gun, Phys. Rev. Lett. **124**, 244801 (2020).

[23] R. Xiang and J. Schaber, Review of recent progress on advanced photocathodes for superconducting RF guns, Micromachines **13**, 1241 (2022).

[24] J. Maxson, L. Cultrera, C. Gulliford, and I. Bazarov, Measurement of the tradeoff between intrinsic emittance and quantum efficiency from a NaKSb photocathode near threshold, Appl. Phys. Lett. **106**, 234102 (2015).

[25] K. Mondal, M. Goawei, L. Cultrera, J. Walsh, R. Bagy, and Y. Yang, Development of sodium potassium antimonide photocathodes for use of coherent electron cooling, in *Proceedings of 6th North American Particle Accelerator Conference, Sacramento, CA, 10-15 Aug 2025* (JACoW Publishing, Geneva, Switzerland, 2025).

[26] M. A. Schmeißer, S. Mistry, H. Kirschner, S. Schubert, A. Jankowiak, T. Kamps, and J. Kühn, Towards the operation of Cs-K-Sb photocathodes in superconducting rf photoinjectors, Phys. Rev. Accel. Beams **21**, 113401 (2018).

[27] L. Cultrera, H. Lee, and I. Bazarov, Alkali antimonides photocathodes growth using pure metals evaporation from effusion cells, J. Vacuum Sci. Technol. B **34**, 011202 (2015).

[28] J. Dube, J. Kühn, C. Wang, S. Mistry, G. Klemz, A. Galdi, and T. Kamps, Triple evaporation growth and photoemission characterization of bialkali antimonide photocathodes, J. Appl. Phys. **138**, 045704 (2025).

[29] J. Kühn, J. Borninkhof, M. Bürger, A. Frahm, A. Jankowiak, T. Kamps, M. Schmeißer, M. Schuster, P. Murcek, J. Teichert, and R. Xiang, UHV photocathode plug transfer chain for the bERLinPro SRF-photoinjector, in *Proceedings of International Particle Accelerator Conference (IPAC'17), Copenhagen, Denmark, 14–19 May, 2017* (JACoW Publishing, Geneva, Switzerland, 2017).

[30] J. Kühn, N. Al-Saokal, M. Bürger, M. Dirsat, A. Frahm, A. Jankowiak, T. Kamps, G. Klemz, S. Mistry, A. Neumann, and H. Plötz, Thermal load studies on the photocathode insert with exchangeable plug for the bERLinPro SRF-photoinjector, in *Proceedings of 19th International Conference on RF Superconductivity, Dresden, Germany* (JACoW Publishing, Geneva, Switzerland, 2019).

[31] S. Mistry, J. Dube, T. Kamps, J. Kuehn, and C. Wang, Evaluation of the in-situ photocathode handling for SRF photoinjector of SEALab, in *Proceedings of the 13th International Particle Accelerator Conference, IPAC'22* (JACoW Publishing, Geneva, Switzerland, 2023), pp. 4240–4242.

[32] C. Wang, J. Dube, A. Galdi, T. Kamps, and J. Kühn, Triple evaporation growth of sodium-potassium-antimonide thin films as photoemission source for electron accelerators, J. Phys. D: Appl. Phys. **59**, 075102 (2026).

[33] G. S. Gevorkyan, S. Karkare, S. Emamian, I. V. Bazarov, and H. A. Padmore, Effects of physical and chemical surface roughness on the brightness of electron beams from photocathodes, Phys. Rev. Accel. Beams **21**, 093401 (2018).

[34] L. Cultrera, S. Karkare, B. Lillard, A. Bartnik, I. Bazarov, B. Dunham, W. Schaff, and K. Smolenski, Growth and characterization of rugged sodium potassium antimonide photocathodes for high brilliance photoinjector, Appl. Phys. Lett. **103**, 103504 (2013).

[35] C. Pennington, E. Echeverria, A. Flint, N. Gonzalez, T. Wu, T. Arias, K. P. Mondal, K. Evans-Lutterodt, M. Gaowei, J. Smedley, *et al.*, Enhanced quantum efficiency from optical interference in alkali antimonide photocathodes: Modeling and experimental results, J. Appl. Phys. **139**, 065305 (2026).

[36] R. Amador, H.-D. Saßnick, and C. Cocchi, Electronic structure and optical properties of Na_2KSb and NaK_2Sb from first-principles many-body theory, J. Phys.: Condens. Matter **33**, 365502 (2021).

[37] R. Follath, M. Hävecker, G. Reichardt, K. Lips, J. Bahrdt, F. Schäfers, and P. Schmid, The energy materials *in-situ* laboratory Berlin (EMIL) at BESSY II, J. Phys.: Conf. Ser. **425**, 212003 (2013).

[38] J. W. Kim and A. Kim, Absolute work function measurement by using photoelectron spectroscopy, Curr. Appl. Phys. **31**, 52 (2021).

[39] A. P. Baddorf, Identifying the secondary electron cutoff in ultraviolet photoemission spectra for work function measurements of non-ideal surfaces, Sci. Rep. **13**, 13452 (2023).

[40] A. H. A. H. Sommer, *Photoemissive Materials: Preparation, Properties, and UIses* (Wiley, New York, 1968).

[41] M. C. Divall, E. Prat, S. Bettoni, C. Vicario, A. Trisorio, T. Schietinger, and C. P. Hauri, Intrinsic emittance reduction of copper cathodes by laser wavelength tuning in an rf photoinjector, Phys. Rev. ST Accel. Beams **18**, 033401 (2015).

[42] I. Bazarov, L. Cultrera, A. Bartnik, B. Dunham, S. Karkare, Y. Li, X. Liu, J. Maxson, and W. Roussel, Thermal emittance measurements of a cesium potassium antimonide photocathode, Appl. Phys. Lett. **98**, 224101 (2011).

[43] M. Abo-Bakr, N. Al-Saokal, W. Anders, Y. Bergmann, K. Bürkmann-Gehrlein, *et al.*, The Berlin Energy Recovery Linac Project BERLinPro - status, plans and future opportunities, in *Proceedings of 63th ICFA Advance Beam Dynamics Workshop on Energy Recovery Linacs, Berlin, Germany* (JACoW Publishing, Geneva, Switzerland, 2019).

[44] T. Kamps, M. Abo-Bakr, B. Alberdi, T. Birke, P. Echevarria, E. Ergenlik, R. Fleischhauer, A. Frahm, H. Huck, G. Klemz, *et al.*, Accelerator physics experiments at the versatile SRF photoinjector of SEALab, in *Proceedings of 14th International Particle Accelerator Conference, Venice, Italy* (JACoW Publishing, Geneva, Switzerland, 2023), pp. 2115–2118.

[45] E. Wang, Y. Hao, Y. C. Jing, V. Litvinenko, I. Pinayev, T. Rao, J. Skaritka, G. Wang, and T. Xin, K2CsSb photocathode performance in QWR SRF gun, in *Proceedings of North American Particle Accelerator Conference (NAPAC'16), Chicago, IL, USA, October 9–14, 2016* (JACoW Publishing, Geneva, Switzerland, 2017).

[46] V. Pavlenko, F. Liu, M. A. Hoffbauer, N. A. Moody, and E. R. Batista, Kinetics of alkali-based photocathode degradation, AIP Adv. **6**, 115008 (2016).

[47] S. K. Mohanty, Development of multi-alkali antimonide photocathodes for high-brightness RF photoinjectors, Ph.D. thesis, Universität Hamburg, 2024.

[48] CST Studio Suite version 2024.05, Dassault Systemes Deutschland GmbH, Vlizy-Villacoublay, France (2024), https://www.3ds.com/products/simulia/cst-studio-suite.

[49] H.-W. Glock, J. Knobloch, A. Neumann, and A. Veléz, Industrial X-ray tomographie as a tool for shape and integrity control of SRF cavities, in *Proceedings of 20th International Conference on RF Superconductivity, East Lansing, MI* (JACOW Publishing, Geneva, Switzerland, 2022), pp. 725–732.

[50] N. Fairley, V. Fernandez, M. Richard-Plouet, C. Guillot-Deudon, J. Walton, E. Smith, D. Flahaut, M. Greiner, M. Biesinger, S. Tougaard, D. Morgan, and J. Baltrusaitis, Systematic and collaborative approach to problem solving using X-ray photoelectron spectroscopy, Appl. Surf. Sci. Adv. **5**, 100112 (2021).